Available online at www.sciencedirect.com
ScienceDirect
Trans. Nonferrous Met. Soc. China 31(2021) 2189−2207
Transactions of Nonferrous Metals Society of China
www.tnmsc.cn

Effects of nano-sized TiB_2 particles and Al_3Zr dispersoids on microstructure and mechanical properties of Al−Zn−Mg−Cu based materials

Hong-yu XIAO[1,2], Yu-gang LI[1,2], Ji-wei GENG[1,2,3], Hong-ping LI[4], Ming-liang WANG[1], Dong CHEN[1,2,3], Zhu-guo LI[5], Hao-wei WANG[1]

1. State Key Laboratory of Metal Matrix Composites, Shanghai Jiao Tong University, Shanghai 200240, China;
2. School of Materials Science and Engineering, Shanghai Jiao Tong University, Shanghai 200240, China;
3. Anhui Provincial Engineering Research Center of Aluminium Matrix Composites, Huaibei 235000, China;
4. Shanghai Aircraft Design and Research Institute, Shanghai 201203, China;
5. Shanghai Key Laboratory of Materials Laser Processing and Modification, Shanghai Jiao Tong University, Shanghai 200240, China

Received 11 September 2020; accepted 6 April 2021

Abstract: The effects of TiB_2 and Zr on the microstructure, aging response and mechanical properties of hot-extruded Al−Zn−Mg−Cu based materials were investigated and compared by multi-scale microstructure characterization techniques. The results showed that proper addition of TiB_2 particles could refine grain size during solidification, promote dynamic recrystallization during extrusion, and inhibit grain growth during solution treatment. Meanwhile, Zr addition had minor influence on the grain refinement during solidification, but could effectively suppress recrystallization and grain growth compared with the Zr-free alloy. Furthermore, the TiB_2 addition could simultaneously enhance the aging kinetics and peak-aged hardness of the materials. Comparatively, Zr addition could also improve the peak-aged hardness with minor effect on the aging kinetics of the materials. Finally, the quench sensitivity, elastic modulus and tensile properties of the materials were compared and studied. Specifically, the relationship between the microstructure and mechanical properties, and the strengthening mechanisms were discussed in detail.

Key words: TiB_2; Al_3Zr; microstructure; aging kinetics; mechanical properties

1 Introduction

Al−Zn−Mg−Cu alloys have been widely applied as structural materials in aerospace, aircraft and automobile industries due to their excellent mechanical properties. For Al−Zn−Mg−Cu alloys, trace elements (i.e., Cr, Zr and Sc) are often introduced to improve the comprehensive properties of the alloys. Generally, the fine Al_3Zr with cubic $L1_2$ structure can precipitate during homogenization treatment in commercial 7xxx Al alloys [1−3]. These uniformly distributed nano-sized dispersoids are coherent with the matrix. Then, they can effectively pin the dislocations and sub-grain boundaries (sub-GBs). As a result, they can exhibit excellent anti-recrystallization behavior and promote the formation of stable refined subgrain structure during the deformation process. There are many reports claiming that a small amount of Zr addition can lead to a combination of high strength, considerable ductility and improved corrosion resistance for the alloys [4−7].

However, the coherent Al_3Zr particles may

Corresponding author: Ming-liang WANG, Tel: +86-21-34202540-206, E-mail: mingliang_wang@sjtu.edu.cn; Dong CHEN, Tel: +86-21-34202540-202, E-mail: chend@sjtu.edu.cn
DOI: 10.1016/S1003-6326(21)65648-0

lose their coherency and become semi-coherency due to precipitate coarsening or migration of GBs [8,9]. These semi-coherent particles may become heterogeneous nucleation sites for η ($MgZn_2$) when the alloys are slowly cooled after the solution treatment [10,11]. Such process can deplete lots of solute atoms and decrease the aging hardening potential of the alloys. Eventually, this may lead to the increased quench sensitivity which is a crucial problem for thicker products.

Recently, in situ TiB_2/Al composites have been studied and considered to be promising structural materials due to their improved mechanical properties, including higher modulus, tensile strength and improved fatigue limit strength [12−14]. TiB_2 is an outstanding reinforcement due to its excellent stiffness, hardness and wear resistance. Besides, TiB_2 particles do not react with Al matrix thermodynamically. Thus, there is the clear and stable TiB_2/Al interface [15]. It was reported by former researchers that the distribution of TiB_2 particles obeyed a log-normal size distribution, and the majority of nano-sized particles were smaller than 100 nm [16]. Meanwhile, TiB_2 particles can serve as the heterogeneous nucleation site for α(Al) during solidification to refine the grain. Also, the nano-sized particles can interact with dislocations and GBs, and influence the recrystallization behaviors. At the same time, the pinning effect of the particles on the GB migration can inhibit the growth of recrystallized grains.

Many researchers have reported the effects of nano-sized reinforcement on the microstructure and properties of the Al−Zn−Mg−Cu based materials [17,18]. However, they have ignored that the sizes of Al_3Zr and TiB_2 particles are of the similar level, and the precise role played by TiB_2 is not fully understood. The present study aimed to study the independent effect of nano-sized TiB_2 particles on the microstructure and mechanical properties of TiB_2/Al−Zn−Mg−Cu composite. Furthermore, the comparison for the effects of Al_3Zr dispersoids and TiB_2 particles on the microstructure and mechanical properties of the materials were also conducted and studied.

2 Experimental

2.1 Materials and heat treatments

Four kinds of alloys and composites with different Zr and TiB_2 contents were investigated. The nominal compositions of these alloys and composites are listed in Table 1.

In the present work, the in situ TiB_2−7085Al composites were fabricated by the salt−metal reaction method, and the detailed procedures could be found in Ref. [19]. The 7085Al and Zr−7085Al alloys were both prepared by the casting method. Two-step homogenization was used for the as-cast alloys and composites. The first step was 350 °C for 12 h, and the second step was 470 °C for 24 h with the heating ramp of 2 °C/min. After homogenization, both alloys and composites were extruded at 430 °C with a ratio of 9:1. Afterwards, the alloys and composites were solutionized at 470 °C for 1 h and then water quenched. At last, the alloys and composites were subjected to the artificial aging treatment at 120 °C for 24 h (T6).

2.2 Vickers hardness, tensile test and end quench test

The Vickers hardness (HV) test was performed on a hardness tester (HVS−30P). For each aged sample, a load of 10 kg with 15 s holding was used in one measurement, and ten measurements were made for each sample to obtain an average value. The tensile test was carried out on a Zwick machine at a stain rate of 1×10^{-3} s^{-1}. The Jominy end quench (JEQ) test was applied to studying the quench sensitivity (QS) characteristics of both alloys and composites. The sample was in the cylinder shape

Table 1 Material design and corresponding nominal compositions of studied materials

Original design	Sample	Content/wt.%					
		Zn	Mg	Cu	Zr	TiB_2	Al
Zr-free alloy	7085Al	7.5	1.5	1.6	0	0	Bal.
Zr-containing alloy	Zr−7085Al	7.5	1.5	1.6	0.15	0	Bal.
In situ 3TiB_2/7085Al composite	3TiB_2−7085Al	7.5	1.5	1.6	0	3.0	Bal.
In situ 7TiB_2/7085Al composite	7TiB_2−7085Al	7.5	1.5	1.6	0	7.0	Bal.

with the size of 125 mm × *d*30 mm. The technical requirement for JEQ test was referred to the GB/T225—2006 standard.

2.3 Microstructure characterization

For the microstructure observation, the sample was ground and polished with the order of SiC paper, diamond paste and colloidal silica. Specifically, for the optical microscopy (OM, Zeiss Imager A1m) characterization, the sample was prepared by anodic coating at 0 °C in the solution of 2.5 vol.% HBF_4 for 30 s at the voltage of 20 V. The field-emission scanning electron microscope (SEM, TESCAN MAIA3) was equipped with an energy dispersive X-ray spectrometry (EDS) system. Unless otherwise noted, the SEM micrograph was taken under the backscattered electron (BSE) imaging mode. On the same SEM, the electron backscattered diffraction (EBSD) study was conducted using a BRUKER e-FlashHR EBSD detector. The EBSD characterization was conducted at 20 kV, and scanned with a step size from 0.2 to 1 μm. The EBSD data were analyzed using CHANNEL 5.0 software. In order to investigate the difference in recrystallization behavior, misorientation angles ranging from 2° to 15° were defined as low-angle GBs (LAGBs), and misorientation angles above 15° as high-angle GBs (HAGBs).

For the transmission electron microscopy (TEM) examination, the sample was thinned to a foil from ~50 to 80 μm, and then eletropolished at −30 °C in the solution of 33 vol.% HNO_3 and 67 vol.% CH_3OH. The thin foil was observed by the TEM (JEM 2100F) operated at 200 kV.

3 Results

3.1 Microstructure in as-cast condition

The optical micrographs of 7085Al and TiB_2−7085Al samples in as-cast condition are shown in Fig. 1. Both 7085Al (Fig. 1(a)) and Zr−7085Al (Fig. 1(b)) samples exhibit the typical dendritic structure. More than 200 grains were measured to determine the average grain sizes of both alloy and composite samples using line intersection method by Image J software. The average grain sizes of 7085Al and Zr−7085Al samples are (198±25) μm and (212±27) μm, respectively. The TiB_2−7085Al samples (Figs. 1(c) and (d)) show equiaxed grains, and the grain sizes of the composites decrease with the increasing TiB_2 content. For example, the average grain size of composite is (52±12) μm when the TiB_2 content is

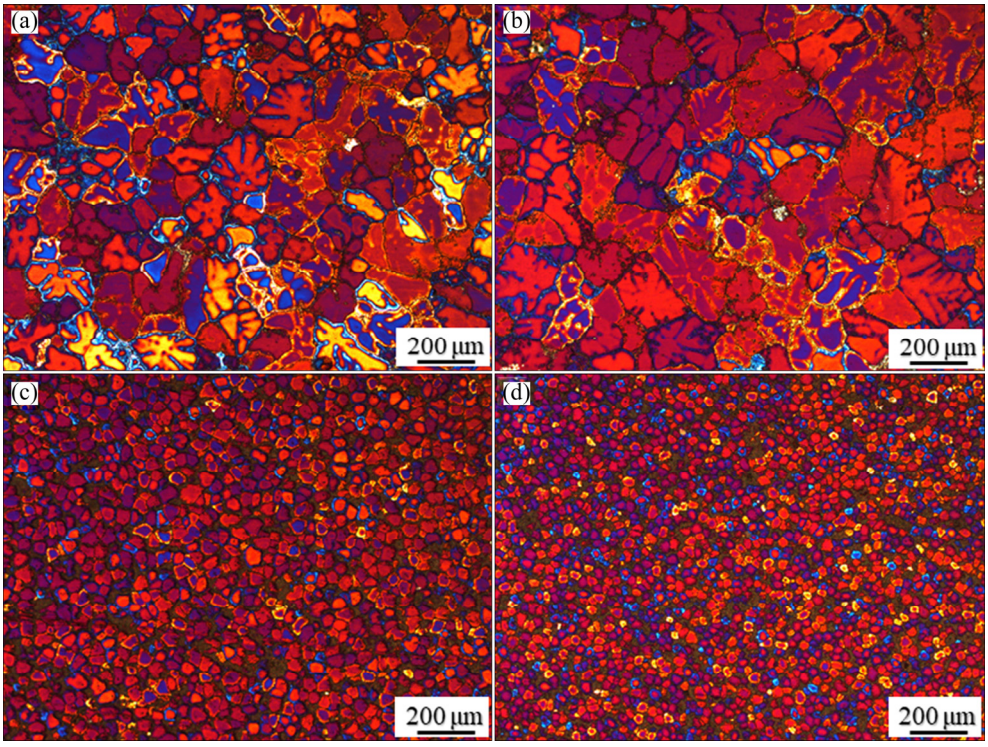

Fig. 1 OM images of alloys and composites in as-cast condition: (a) 7085Al; (b) Zr−7085Al; (c) 3TiB_2−7085Al; (d) 7TiB_2−7085Al

3 wt.% (Fig. 1(c)), and it deceases to (38±7) μm when the TiB_2 content increases to 7 wt.% (Fig. 1(d)). The similar results were also reported for TiB_2/Al composites in Refs. [20,21].

The EDS element mapping analyses of both alloy and composite samples in the as-cast condition are exhibited in Fig. 2. In the Zr−7085Al sample (Fig. 2(a)), most second phases are located along GBs. The element mapping analyses indicate that there are three kinds of second phases marked as A, B and C, accordingly. Phase A mainly contains Al, Zn, Mg and Cu elements, and their corresponding contents (at.%) are 24.47, 30.04, 20.81 and 24.68, respectively. Consequently, Phase A is identified as *T* phase (AlZnMgCu). Phase B mainly contains Al, Cu and Fe with the corresponding contents (at.%) of 69.24, 18.82 and 10.97, respectively, and is interpreted as Al_7Cu_2Fe phase. Phase C mainly contains Al, Cu and Mg with the corresponding contents (at.%) of 51.08, 24.02 and 24.9, respectively. Accordingly, Phase C is probably interpreted as *S* (Al_2CuMg) phase. Normally, *T* and *S* phases can be formed during solidification when the mole ratio of Zn/Mg is larger than 2.2:1 [22]. Both phases can be dissolved into the matrix under proper heat treatment. Comparably, Al_7Cu_2Fe phase is difficult to be dissolved into the matrix. This phase is hard and fragile to be detrimental to mechanical properties of the material [23].

In the 3TiB_2−7085Al sample (Fig. 2(b)), TiB_2 particles are aggregated at GBs mainly due to the push effect by the advancing solid−liquid interface [24]. The TiB_2 particles have minor influence on the types of second phase on GBs. Notably, most second phases are found to be covered by TiB_2 clusters. These clusters can act as particle shells, and hinder the dissolution of second phase during solution treatment [25].

3.2 Characterization of TiB_2 particles and Al_3Zr dispersoids

The TEM images of TiB_2 particles and Al_3Zr dispersoids in the as-quenched condition are shown in Fig. 3. In detail, Fig. 3(a) shows the TEM image of nano-sized TiB_2 particles. TiB_2 particles with the cubic shape are randomly distributed. The high resolution transmission electron microscopy (HRTEM) image of TiB_2 particles along $[110]_{Al}$ and the corresponding Fast Fourier Transformation (FFT) pattern are exhibited in Fig. 3(b).

The HRTEM image shows a clear interface between the Al matrix and TiB_2 particles, indicating that no interfacial reaction has occurred at the interface. The size distribution of TiB_2 particles is exhibited in Fig. 3(c). Notably, most TiB_2 particles

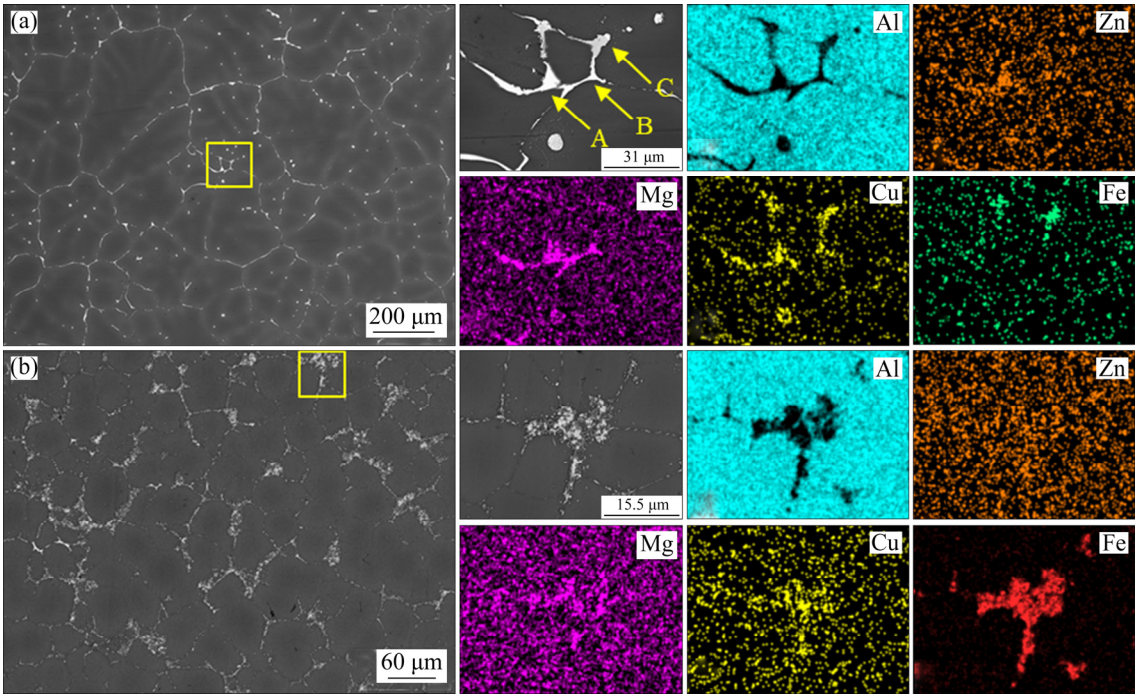

Fig. 2 BSE micrograph of Zr−7085Al sample and corresponding element mapping analyses with three phases marked with A, B and C (a), and BSE micrograph of 3TiB_2−7085Al sample and corresponding element mapping analyses (b) in as-cast condition

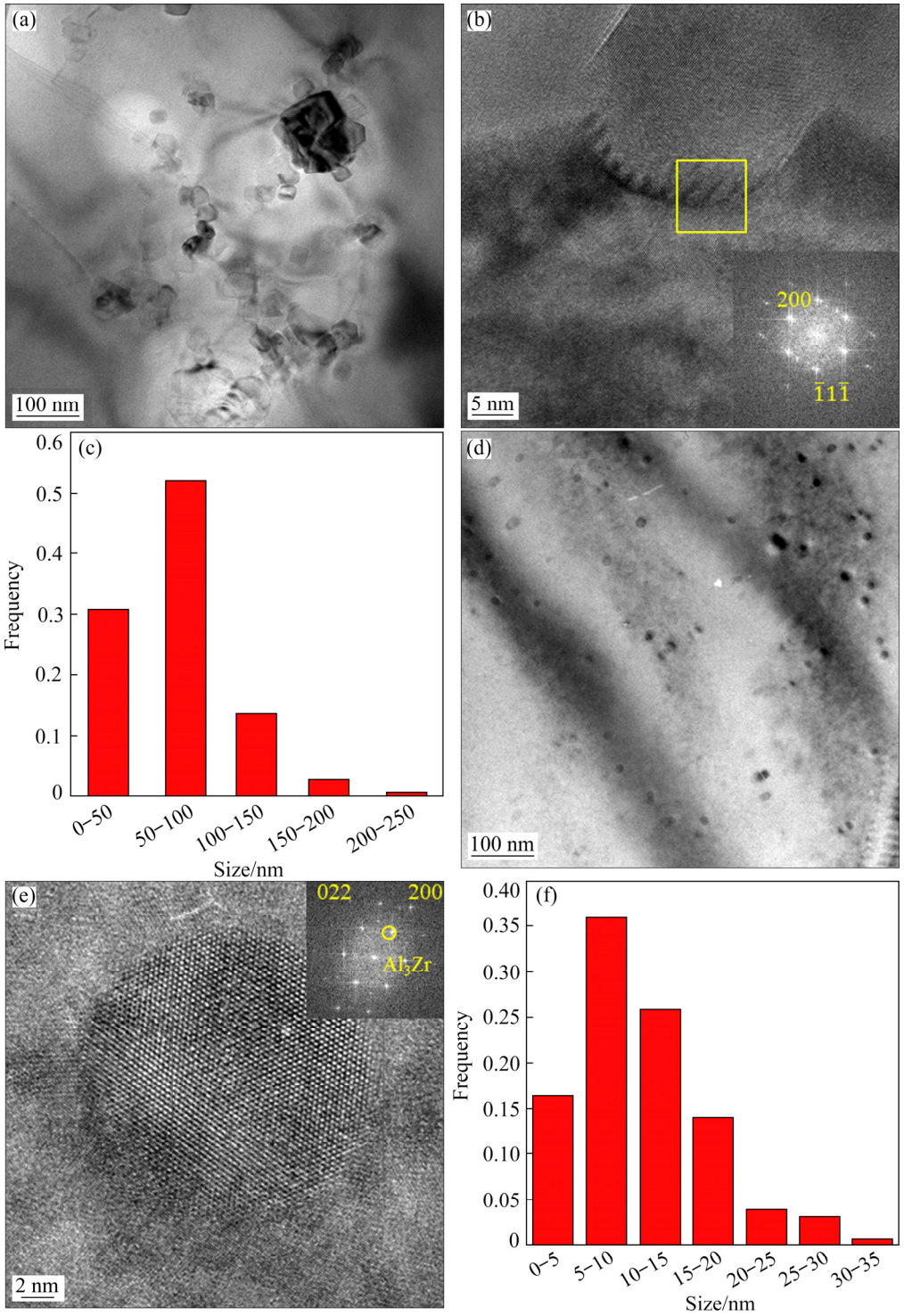

Fig. 3 TEM image of TiB_2 particles at as-quenched state (a), HRTEM image of TiB_2 particle along $[110]_{Al}$ with FFT pattern (b), size distribution of TiB_2 particles (c), TEM image of Al_3Zr dispersoids (d), HRTEM image of Al_3Zr along $[111]_{Al}$ with FFT pattern (e), and size distribution of Al_3Zr dispersoids (f)

are ≤100 nm, and the average size of the particles is 80 nm. In comparison, Fig. 3(d) shows the TEM image of Al_3Zr dispersoids. The Al_3Zr dispersoids with the sphere shape are found to distribute uniformly inside the grain. The HRTEM image along $[111]_{Al}$ and the corresponding FFT pattern of Al_3Zr dispersoids are exhibited in Fig. 3(e). The size distribution of Al_3Zr dispersoids is exhibited in Fig. 3(f), and the average size of Al_3Zr dispersoids is measured to be 20 nm.

3.3 Recrystallization behavior during extrusion and heat treatment

The EBSD maps of all samples along the extrusion direction (ED) at as-extruded and T6 states are shown in Fig. 4. There are deformed, sub-structured and recrystallized grains according to the mean grain misorientation. The corresponding recrystallization fraction and average grain size are calculated and listed in Table 2. Apparently, the dynamic recrystallization has occurred during hot extrusion in both alloys and composites. In the as-extruded condition, both recrystallization fraction and average grain size of 7085Al sample are much larger than those of Zr−7085Al sample (Table 2). For the composites, the average grain size decreases as the TiB_2 content increases. For example, the average grain size is 17.7 μm at 3 wt.% TiB_2, and it decreases to 8.1 μm at 7 wt.% TiB_2 (Table 2). Nevertheless, the recrystallization fraction decreases as the content of TiB_2 increases. Specifically, the recrystallization fractions are 14.9% for $3TiB_2$−7085Al and 10.2% for $7TiB_2$−7085Al.

After the T6 heat treatment, the recrystallization fraction and grain size of 7085Al sample increase significantly. Nevertheless, the recrystallization fraction and grain size of Zr−7085Al remain relatively stable compared with the 7085Al sample

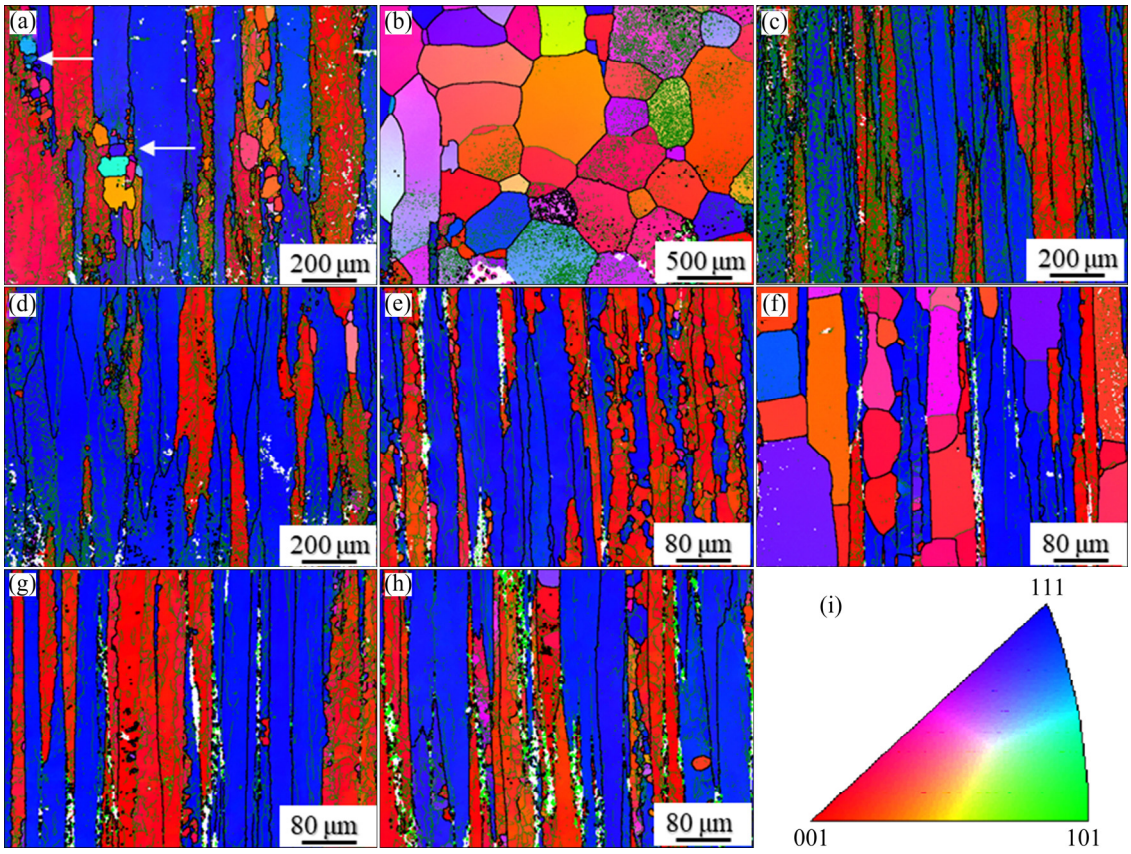

Fig. 4 EBSD maps showing grain structures in as-extruded (a, c, e, g) and T6 (b, d, f, h) conditions (TiB_2 colored as lime green): (a, b) 7085Al; (c, d) Zr−7085Al; (e, f) $3TiB_2$−7085Al; (g, h) $7TiB_2$−7085Al; (i) IPF orientation map

Table 2 Recrystallization fractions and average grain sizes of samples in as-extruded and T6 conditions

Sample	Recrystallization fraction/%		Average grain size/μm	
	As-extruded	T6	As-extruded	T6
7085Al	10.9	68	38.9	86.8
Zr−7085Al	3.7	5.5	31.1	32.5
$3TiB_2$−7085Al	14.9	44.4	17.7	22.7
$7TiB_2$−7085Al	10.2	10.9	8.1	8.2

(Table 2). Regarding the composites, the ability to inhibit grain growth increases with elevating TiB_2 content (Table 2). For example, the recrystallization fraction and average grain size for $3TiB_2$−7085Al sample have increased to 44.4% and 22.7 μm (Table 2), respectively. However, they are rarely altered for the $7TiB_2$−7085Al sample after T6 treatment (Table 2). In conclusion, the proper TiB_2 addition can promote recrystallization and effectively stabilize grain structure. Meanwhile, Al_3Zr dispersoids can inhibit recrystallization and stabilize grain structure.

3.4 Age hardening kinetics

The age hardening curves of the alloys and composites are shown in Fig. 5. The hardness of 7085Al sample shows a sharp increase in the first 6 h, and increases slowly for the longer aging time. The aging time for the 7085Al alloy to reach its peak-aged hardness is 22 h. There are similar aging behaviors for the Zr−7085Al sample compared with the 7085Al sample. The Zr−7085Al sample also shows a rapid increase in the first 6 h, and a slow increase for the longer aging time. The peak aging time is 24 h, which is a little longer than that of the 7085Al sample, although the peak-aged hardness is higher for the Zr−7085Al sample. For the TiB_2−7085Al samples, the hardness still increases rapidly in 6−12 h compared with the 7085Al alloys. Furthermore, the hardened speed is accelerated as the TiB_2 content increases. The peak aging time decreases with the increasing TiB_2 content. Specifically, the peak aging time is 18 h for the $3TiB_2$−7085Al sample and 14 h for $7TiB_2$−7085Al sample. The peak-aged hardness increases as the TiB_2 content increases. The peak aging time is shortened, and the peak-aged hardness is improved for the TiB_2−7085Al samples over the 7085Al and Zr−7085Al samples. Conclusively, the Zr addition has little effect on the aging kinetics of 7085Al sample, but can improve the peak-aged hardness. Comparably, the TiB_2 addition can simultaneously accelerate the aging kinetics and enhance the peak-aged hardness.

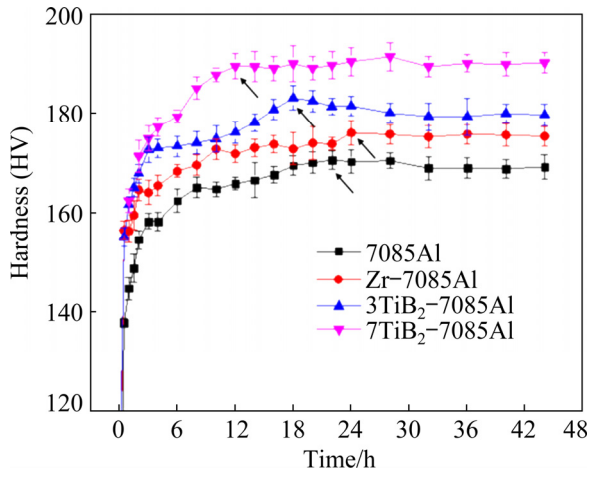

Fig. 5 Age hardening curves of (Zr−)7085Al and TiB_2−7085Al samples with peak-aged hardness marked by black arrows

The bright field (BF), selected area electronic diffraction (SAED) and HRTEM images of the alloys and composite aged for 6 h (the under-aged state) are exhibited in Fig. 6. The diffraction spots from the Al matrix have been indexed (Figs. 6(c), (f) and (i)). The η' phase can be easily identified as spots at 1/3 and 2/3 of the matrix reflection $(2\bar{2}0)$ (Figs. 6(c), (f) and (i)), and the GPII zone is referred to spot at 1/2 of the matrix reflection $(3\bar{1}\bar{1})$ [26] . For the 7085Al sample (Figs. 6(a), (b) and (c)), the main strengthening phases in the grain are η' phase with some GPII zones at 6 h aging. The HRTEM images taken with the incident electron beam along the [112] zone axis of the Al matrix and the corresponding FFT pattern have confirmed the results. The situations are almost the same when it comes to the Zr−7085Al sample (Figs. 6(d), (e) and (f)). For the $7TiB_2$−7085Al composite (Figs. 6(g), (h) and (i)), the main strengthening phases in the matrix are η' phase with few GPII zones. The corresponding HRTEM image and SAED pattern convince the results. Clearly, the diffraction spots for GPII are quite weaker compared to those of the alloys, and almost GPII can rarely be found in the HRTEM image (Fig. 6(i)).

The BF and SAED images of the alloys and composite at the peak-aged state are shown in Fig. 7. Fine strengthening phases with the size of 3−6 nm are well-distributed inside the grain for both alloys and composite. The SAED images (Figs. 7(b), (d) and (f)) indicate that the main strengthening phases are η' phase with few GPII zones for the alloys and composite. Generally, GPII zones are formed after quenching from temperatures above 450 °C and aging at temperatures above 70 °C [26]. GPII zones can be formed as precursors to the metastable η' phase. The main strengthening phases are η' phase with some GPII zones for the alloys, but are η' phase

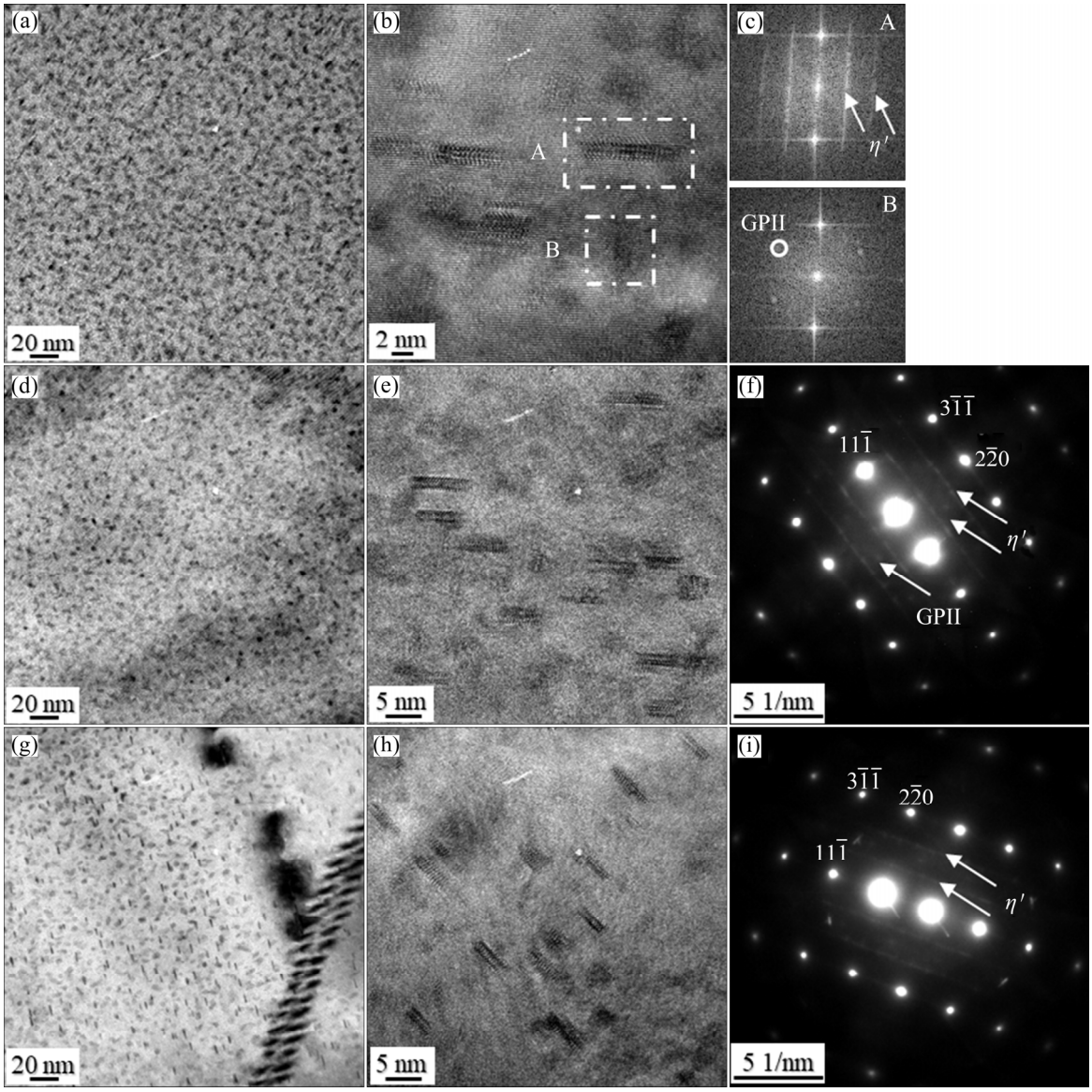

Fig. 6 BF (a, d, g), HRTEM (b, e, h) images and SAED patterns (c, f, i) of alloys and composite aged for 6 h (under-aged state): (a−c) 7085Al; (d−f) Zr−7085Al; (g−i) 7TiB_2−7085Al

with few GPII zones for the composite at 6 h aging. It can be inferred that GPII zones should exist during early stage of aging, and have almost transformed into η' phase for the composite.

As the aging time proceeds, GPII zones in the alloys continue to transform into η' phase. Eventually, the main strengthening phases for both the alloys and composite at the peak-aged state are η' phase with few GPII zones. The accelerated aging kinetics by TiB_2 addition was also reported by DU et al [27], which was mainly attributed to the abundant dislocations caused by TiB_2 particles. On one hand, the dislocations produced during extrusion may be pinned and stabilized by TiB_2 particles even after solution treatment. On the other hand, the formation of dislocations around the particles should inevitably occur in the composite due to the difference in coefficients of thermal expansion (CTEs) between the particle and matrix. These increased dislocations should serve as fast diffusion paths and traps for solute atoms during the aging treatment. As a result, the aging kinetics is enhanced, and the aging time to reach peak-aged hardness is shortened.

3.5 Mechanical properties

3.5.1 Quench sensitivity relative to hardness

The quench sensitivities relative to hardness of (Zr−)7085Al and TiB_2−7085Al samples were investigated by the JEQ test [28,29]. Figure 8(a)

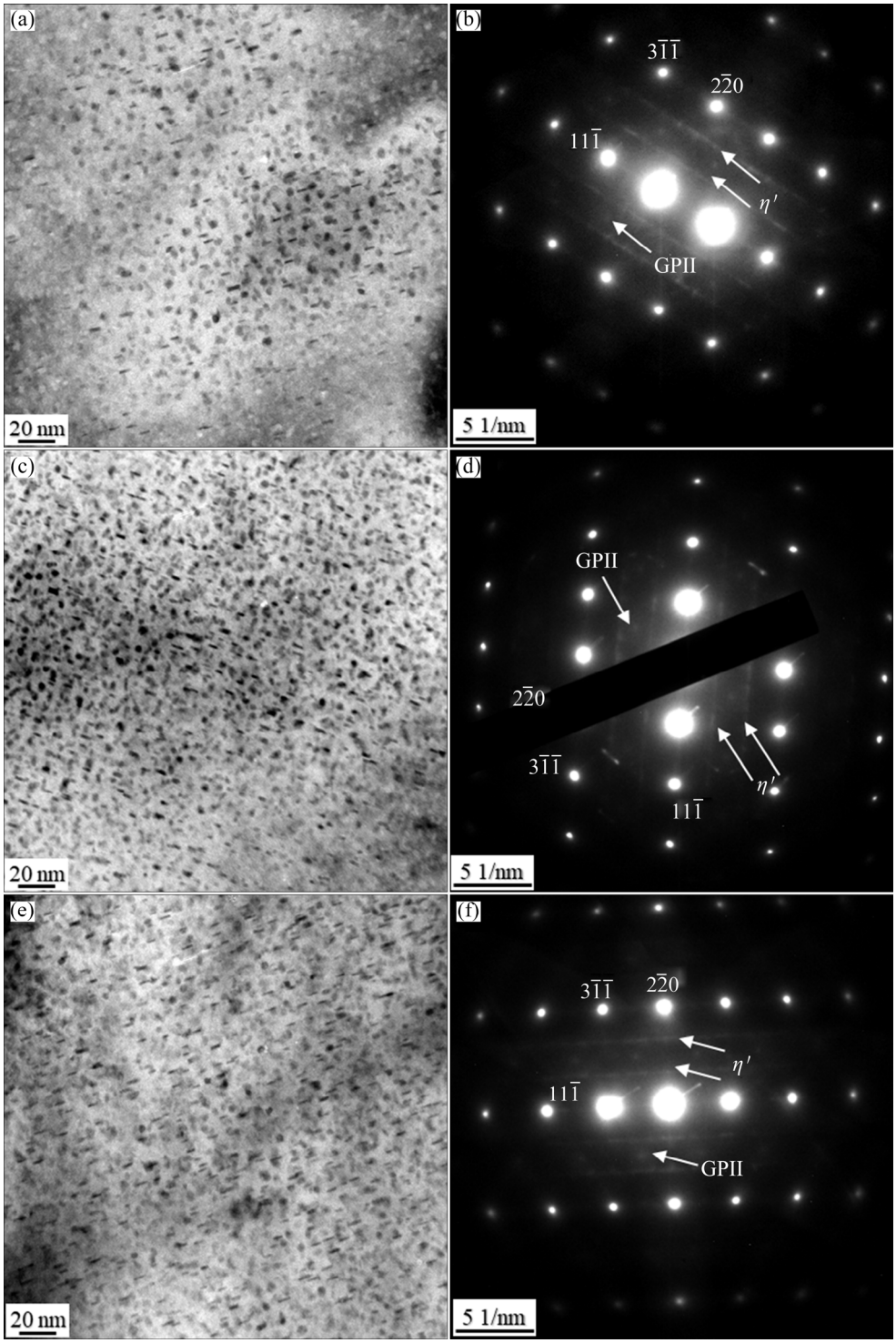

Fig. 7 BF images (a, c, e) and SAED patterns (b, d, f) of alloys and composite at T6 state: (a, b) 7085Al; (c, d) Zr−7085Al; (e, f) 7TiB_2−7085Al

exhibits the hardness changes of alloys and composites in the T6 condition on dependence of the JEQ distance. The hardness of 7085Al sample has merely changed with the increasing JEQ distance. Comparably, the hardness of Zr−7085Al sample decreases first, and then remains stable as the JEQ distance increases. For the TiB_2−7085Al samples, the hardness shows the similar tendency with the Zr−7085Al sample. For the Zr−7085Al sample, the hardness declines when the JEQ distance ranges from 0 to 75 mm. For the 3TiB_2−7085Al sample, the hardness declines when the

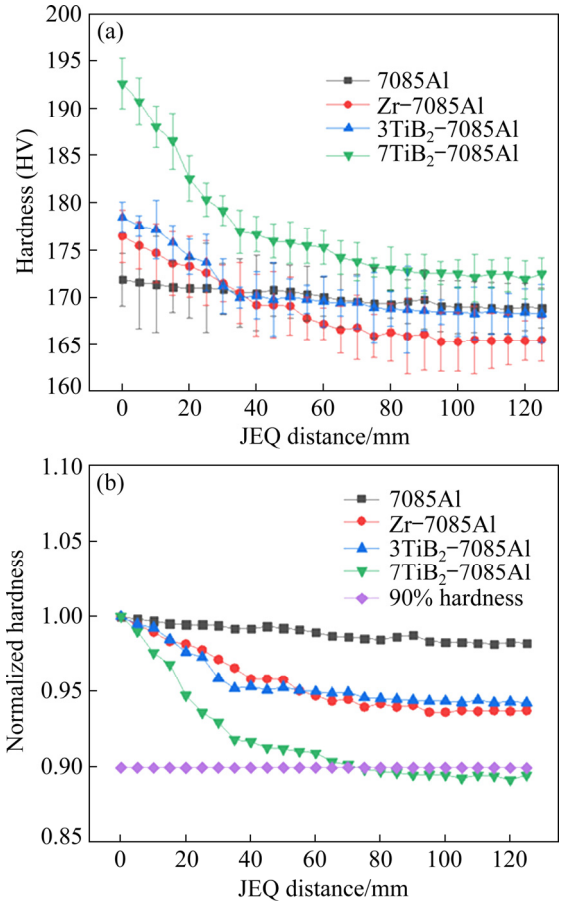

Fig. 8 Hardness profiles of alloys and composites in T6 condition (a) and normalized hardness (b) on dependence of JEQ distance (D)

JEQ distance ranges from 0 to 75 mm. For the $7TiB_2$−7085Al sample, the decline range is from 0 to 90 mm, whose reduced rate is larger than that of the Zr−7085Al sample. Normally, the quench sensitivity can be simply described by the depth of age hardening layer, which is evaluated by the distance where a 90% hardness retention value is achieved [30]. The normalized hardness change is shown in Fig. 8(b). In detail, the depths corresponding to 90% of the maximum as-aged hardness measured by the JEQ test are 90 mm for the $7TiB_2$−7085Al sample, and the depths are all >125 mm for other samples.

The addition of either Zr or TiB_2 particles can enhance the quench sensitivity of the matrix alloy, and the quench sensitivity increases as the TiB_2 content increases for the composites. Generally, the quench sensitivity of the alloys and composites can be sequenced as: $7TiB_2$−7085Al>Zr−7085Al≈$3TiB_2$−7085Al >7085Al.

Generally speaking, the quench sensitivity for Al−Zn−Mg−Cu based materials is related to coarse phases (i.e., $\eta(MgZn_2)$, $S(Al_2CuMg)$ and $T(Al_2Mg_3Zn_3)$) precipitating during the slow quenching. The GBs, sub-GBs and dispersoids (i.e., Cr or Zr bearing intermetallic particles) can often act as effective nucleation sites for these quench-induced phases [31,32]. As a result, a large number of solutes are depleted, which should decrease the aging hardening ability during subsequent aging. For the 7085Al sample, there are few dispersoids acting as nucleation sites for quench-induced phases. Furthermore, the average grain size for this alloy is much larger than those of other samples. Therefore, the average length of GB per unit area is much smaller for the 7085Al sample. In Fig. 9(a), only a small part of coarse phases can be observed on the (sub)-GBs. Nearly no coarse phase can be found inside the grain. As a result, the amount of coarse phases precipitating during slow quenching is much less, and most solute atoms are kept for subsequent aging. Consequently, the hardness shows almost no decline for the 7085Al sample even at D=125 mm. For the Zr−7085Al sample, Al_3Zr dispersoids lost their coherency with the matrix can serve as nucleation sites for η ($MgZn_2$) phase during slow quenching (Fig. 9(b)). Meanwhile, the grain size of the Zr−7085Al sample is much smaller than that of 7085Al sample. Nucleation sites on the GBs per unit area of the Zr−7085Al sample are much more than those of the 7085Al sample. Eventually, the Zr−7085Al sample is more quench sensitive. For the composites, the quench sensitivity increases with the increasing TiB_2 content. The elevated quench sensitivity can be mainly attributed to two facts. Firstly, the average grain size decreases as TiB_2 content increases (Figs. 9(c) and (d)), which provides more nucleation sites for coarse phases. Secondly, the TiB_2 addition should result in the higher dislocation density. These dislocations may provide effective heterogeneous nucleation sites during slow quenching. The addition of reinforcement should often increase the quench sensitivity of the composite as reported in Refs. [33,34]. Interestingly, with 3 wt.% TiB_2 addition, the quench sensitivity of the composite can be similar to the Zr-containing alloy. Besides, 7085 Al alloy is a new generation Al alloy with lower quench sensitivity but lower tensile properties compared with other 7xxx alloys. This

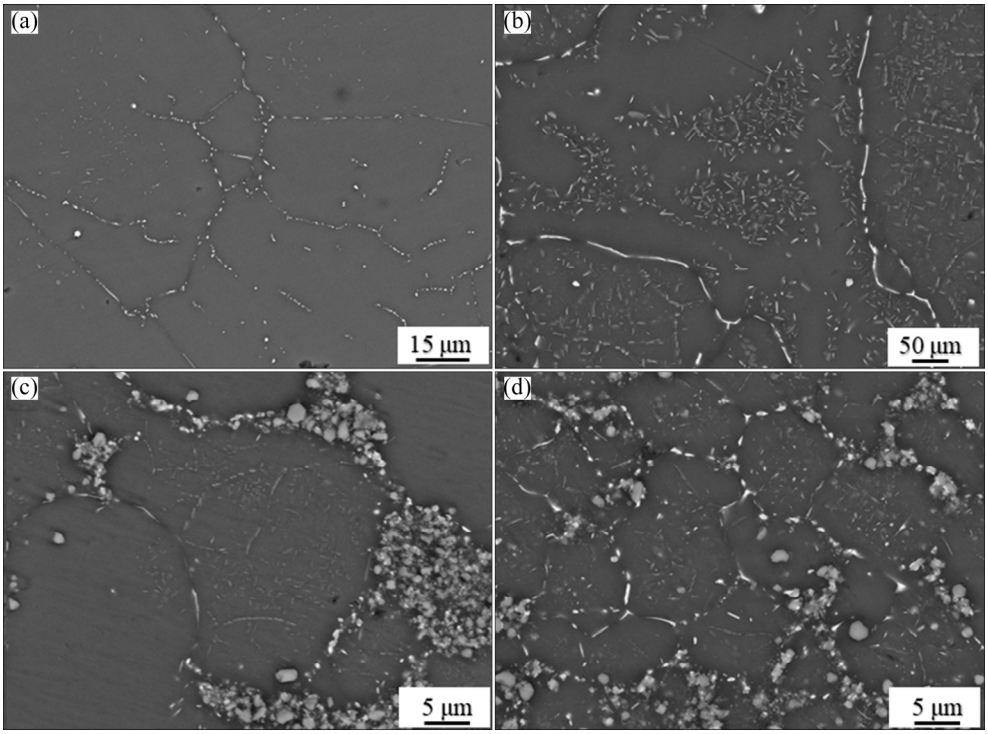

Fig. 9 SEM images of alloys and composites at D=125 mm: (a) 7085Al; (b) Zr−7085Al; (c) 3TiB_2−7085Al; (d) 7TiB_2−7085Al

work makes us a better understanding of the relationship among alloy composition (Zr and TiB_2), quench sensitivity and tensile properties or hardness on the 7085Al based materials.

3.5.2 Tensile properties and elastic modules

Figure 10 shows the engineering stress−strain curves of the (Zr)−7085Al and TiB_2−7085Al samples at T6 state. The yield strength (YS), ultimate tensile strength (UTS) and elongation to failure (EL) of alloys and composites at T6 state are summarized in Table 3. The YS and UTS are 415.7 and 514.7 MPa for the 7085Al sample, respectively. Comparably, the YS and UTS are 591.2 and 633.6 MPa for the Zr−7085Al sample, respectively, which are improved remarkably over those of the 7085Al sample. For the composites, the YS and UTS increase, and the EL decreases as TiB_2 content increases. Specifically, the YS and UTS are 526.9 and 584.2 MPa, respectively, and the EL is 12.9% for the 3TiB_2−7085Al sample. For the 7TiB_2−7085Al sample, the YS and UTS are 607.8 and 666.1 MPa, respectively, and the EL is 7.6%. Among these alloys and composites, the 7TiB_2−7085Al sample exhibits the largest YS and UTS, and the smallest EL. In comparison, the 7085Al sample shows the smallest YS and UTS.

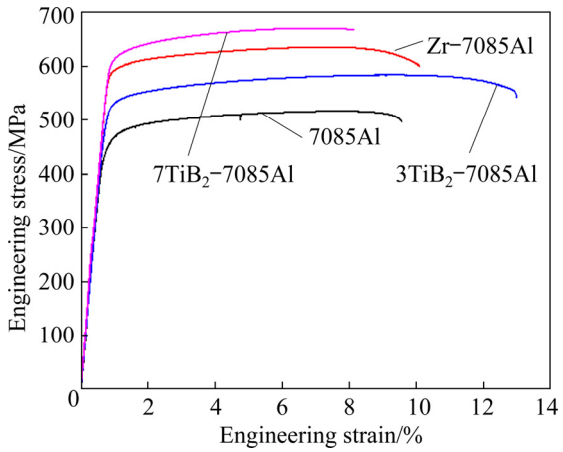

Fig. 10 Engineering stress−strain curves of alloys and composites at T6 state

Interestingly, the Zr−7085Al and 7TiB_2−7085Al samples show almost the same tensile properties, although the 7TiB_2−7085Al sample has a bit larger UTS than the Zr−7085Al sample.

The elastic moduli of the (Zr)−7085Al and TiB_2−7085Al samples at T6 state are also listed in Table 3. The elastic moduli are 69.2 GPa for the 7085Al sample, and 69.8 GPa for the Zr−7085Al sample. Both alloys have similar elastic modulus. For the composites, the elastic modulus increases as the TiB_2 content increases. Specifically, the elastic

moduli are 72.6 GPa for the 3TiB_2−7085Al sample and 75.9 GPa for the 7TiB_2−7085Al sample. In conclusion, the addition of Zr can significantly improve the tensile properties with little effect on the elastic modulus of the material. In comparison, the addition of TiB_2 particles can enhance both the tensile properties and elastic modulus of the material.

Table 3 Tensile properties of alloys and composites at T6 state

Sample	Elastic modulus/ GPa	YS/ MPa	UTS/ MPa	EL/ %
7085Al	69.2±0.2	451.7±5.3	514.7±4.3	9.6±0.4
Zr−7085Al	69.8±0.4	591.2±6.3	633.6±4.6	10.1±0.2
3TiB_2−7085Al	72.6±0.2	526.9±1.4	584.2±0.6	12.9±0.1
7TiB_2−7085Al	75.9±0.1	607.8±2.7	666.1±4.9	7.6±0.7

Figure 11 exhibits the typical tensile fracture morphologies of the alloys and composites at T6 state. A lot of large flats on the fracture surface and cracks exist along the GBs as shown in Fig. 11(a). It can be inferred that the 7085Al sample shows the typical intergranular fracture. For the Zr−7085Al sample (Fig. 11(b)), a large number of dimples are presented on the fracture surface, suggesting the transgranular characteristics of fine dimples. For the composites (Figs. 11(c) and (d)), the dimples become smaller but shallower as the TiB_2 content increases. Simultaneously, more TiB_2 clusters are observed on the fracture surface, which should deteriorate the tensile properties to some extent. It was reported by NAFAR et al [35] that the damage growth rate of composite with higher clustering degree was significantly higher than those of composites with lower clustering degree. This may explain that the EL decreases with the increasing TiB_2 content.

4 Discussion

4.1 Effect of Zr and TiB_2 particles on recrystallization and grain growth

4.1.1 Effect of Zr and TiB_2 particles on recrystallization

In Fig. 4 and Table 2, the recrystallization fraction of 7085Al sample at as-extruded state is higher than that of the Zr−7085Al sample. Dynamic recovery often occurs in Al alloy during hot deformation due to its high stacking fault energy, which can reduce the stored energy for recrystallization. Nevertheless, the dynamic recrystallization

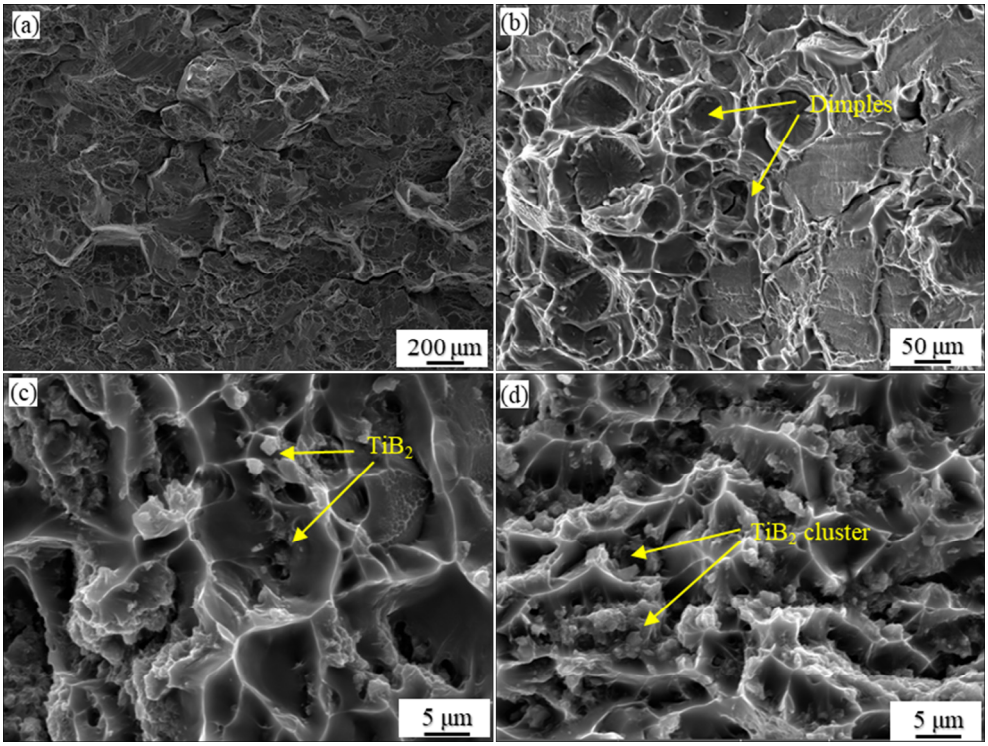

Fig. 11 Fracture morphologies of alloys and composites: (a) 7085Al; (b) Zr−7085Al; (c) 3TiB_2−7085Al; (d) 7TiB_2−7085Al

can still happen under some conditions [36−38]. In the 7085Al sample, the GBs have developed into serrations (white arrows in Fig. 4(a)), which can serve as the actual nucleation sites for recrystallization [39]. Apparently, most recrystallized grains are along the original GBs. This is probably deemed as the discontinuous dynamic recrystallization. In this case, the boundary corrugations or serrations should occur due to dislocation density gradients developed near the original GBs because of the incompatibilities between grains. Under this condition, the GB slide can take place, which should give rise to the development of additional inhomogeneous strains. As a result, this can enhance the driving force for recrystallization, and recrystallization fraction is 10.9%. For the Zr−7085Al sample, the recrystallization fraction is 3.7%, which is smaller than that of 7085Al sample. This is attributed to the pinning effect of Al_3Zr precipitating during homogenization treatment. The commonly used form of Zener pinning effect (P_Z) is formulated as [39]

$$P_Z=\frac{3f_V\gamma}{2r} \tag{1}$$

where r is the particle radius; f_V is the volume fraction of particle; γ is the interfacial energy.

Apparently, the pinning effect increases with the increasing volume fraction and decreasing radius of the particles. Al_3Zr dispersoids have notable pinning effect on the rearrangement of dislocations and (sub)-GB migration due to the smaller size and higher volume fraction [40]. For the composites, a part of TiB_2 particles are found to aggregate on the GBs to form clusters as shown in Fig. 2(b). Some of these clusters are covered with the second phases. Large deformation heterogeneities are typically formed near these clusters or bands during deformation, which should promote the particle stimulated nucleation (PSN) effect [41,42]. In this condition, the accumulation of misorientation by the rapid LAGB migration is sufficient to generate the necessary HAGB. This forms a new grain nucleus, which may then either stagnate, or grow to produce a recrystallized grain. In Fig. 12, higher recrystallization fraction (16.9%) and orientation gradients are observed around particle clusters than those of the deformed matrix for $7TiB_2$−7085Al sample. Recrystallized grains (blue) are mostly distributed around TiB_2 particles (lime green), and should be attributed to the PSN effect (Fig. 12(a)). ZHANG et al [43] investigated the effect of second-phase particles on a particle-containing Al alloy by 3D serial sectioning. They found that 90% of recrystallization nuclei were caused by clusters and bands of large intermetallic particles. The generation of HAGBs through rapid LAGB migration occurs and the HAGB fraction is calculated to be 68.5% (Fig. 12(b)). For the composite, it is found that the recrystallization fraction decreases as the content of TiB_2 increases. This can partly be explained by the pinning effect of TiB_2 particles. Once the dynamic recrystallization occurs along TiB_2 clusters and bands, the recrystallized grains grow by consuming the deformed zones. For the $3TiB_2$−7085Al sample, the

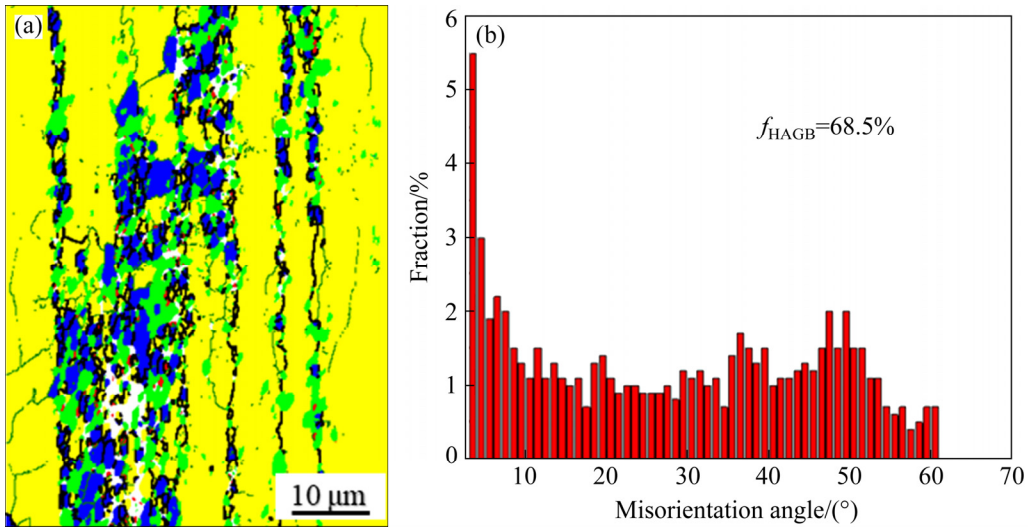

Fig. 12 Distributions of deformed (in red), sub-structured (in yellow) and recrystallized (in blue) grains with TiB_2 in lime green (a) and corresponding misorientation angle distribution (b) for $7TiB_2$−7085Al sample

nucleation sites are less due to small number in TiB_2 clusters and bands. Meanwhile, the pinning effect is also weak. For the 7TiB_2−7085Al sample, the nucleation sites are more than those of the 3TiB_2−7085Al sample, but the pinning effect is much stronger. As a result, most recrystallized grains are pinned by TiB_2 as shown in Fig. 12(a). Consequently, the recrystallization fraction of the 7TiB_2−7085Al sample is smaller than that of the 3TiB_2−7085Al sample.

4.1.2 Effect of Zr and TiB_2 particles on grain growth

In Fig. 4 and Table 2, the recrystallization fractions and grain sizes of 7085Al and 3TiB_2−7085Al samples increase remarkably after the solution treatment, while those of the Zr−7085Al and 7TiB_2−7085Al samples remain stable at some extent. The increase in recrystallization fraction and grain size can be explained in terms of GB migration. Taking the Zener pining effect into consideration, the GB migration rate (v) can be formulated as follows [44]:

$$v=M_0\exp(-\frac{Q}{RT})(P_D^{Rex}-P_Z-P_C) \quad (2)$$

where M_0 is a constant of boundary mobility; Q is the apparent activation energy; P_D^{Rex} is the driving force for recrystallization and can be approximated as a function of dislocation density (ρ); P_C is retarding pressures due to boundary curvature; R is mole gas constant; T is thermodynamic temperature.

Recrystallization and grain growth need the migration of GB, which should correspond to $P_D^{Rex}-P_Z-P_C>0$. During solution treatment, the temperature (470 °C) is much higher than the extrusion temperature (350 °C). The driving force for GB migration P_D^{Rex} is supposed to decrease due to the reduced dislocation density by recovery. However, P_Z is considered to increase as the temperature elevates according to the Zener pinning effect. This is because γ increases as the temperature evaluates, whereas r remains the same due to the stability of Al_3Zr dispersoids and TiB_2 particles. P_C also increases as the temperature increases.

For the 7085Al and 3TiB_2−7085Al samples, there is little pinning effect or the pinning effect (P_Z) is much less compared with the driving force for recrystallization. Hence, the recrystallization fraction is higher at the as-extruded state. During solution treatment, the recrystallization fraction and grain size increase remarkably due to the lacking of pining effect. For the Zr−7085Al and 7TiB_2−7085Al samples, P_D^{Rex} decreases, and P_Z and P_C both increase as the temperature elevates. This means that the whole driving force is less at solution temperature than that at the extruded temperature. Therefore, the structure can be pinned by stable and fine particles as temperature increases, as shown in Fig. 13(b). Accordingly, the recrystallization fraction and grain size remain stable after the solution treatment.

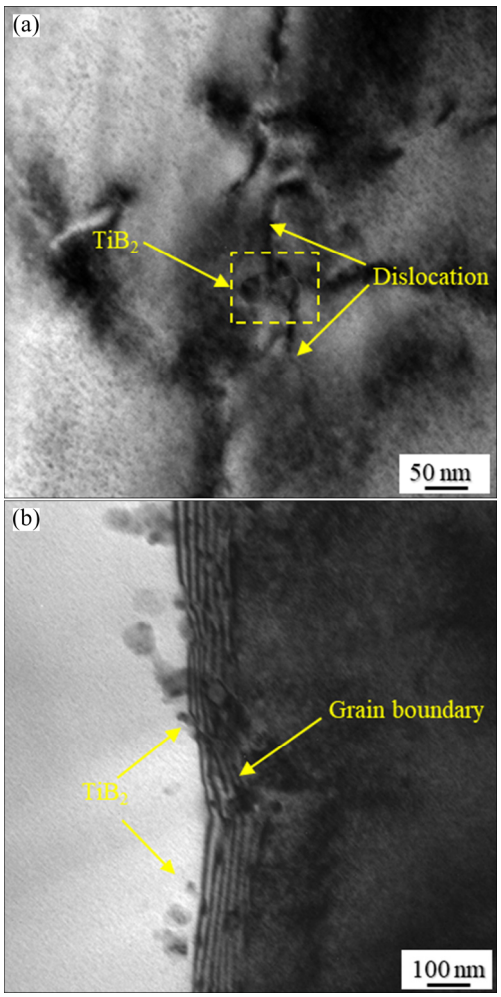

Fig. 13 TEM images showing precipitates nucleating on dislocations produced by TiB_2 particles (a) and GB pinning by TiB_2 particles (b)

4.2 Effect of Zr and TiB_2 particles on mechanical properties

4.2.1 Tensile properties

The Zr addition has significantly enhanced the yield strength and ultimate tensile strength of alloy

by 140.5 and 118.9 MPa, respectively. Comparably, increments of the yield strength and ultimate tensile strength of the composite increase with the elevated TiB_2 content, ranging from 75.2−156.1 MPa and 69.5−151.4 MPa, respectively. Generally, the Zr−7085Al and 7TiB_2−7085Al samples show almost the same tensile properties. The underlying mechanisms of strength enhancement by Zr and TiB_2 addition should include Orowan strengthening ($\Delta\sigma_{Orowan}$), dislocation strengthening ($\Delta\sigma_d$) and grain-boundary strengthening ($\Delta\sigma_g$) [45−47]. Meanwhile, the value of each strength enhancement is estimated, and the proportion of each strength enhancement is calculated.

The addition of Zr and TiB_2 can remarkably stabilize the grain size (Table 2). The high density of GBs can effectively strengthen the materials by impeding dislocation movement and dislocation propagation to adjacent grains. Accordingly, the GB strengthening ($\Delta\sigma_g$) should be taken into consideration. Based on Hall−Petch strengthening relationship, the finer grain size can increase the yield strength in materials, and the relationship can be described as

$$\Delta\sigma_g = k\left(\frac{1}{\sqrt{d}} - \frac{1}{\sqrt{d}_0}\right) \tag{3}$$

where d and d_0 are the average grain sizes (m) of composite and 7085Al, respectively; k is a constant related to material and is equal to about 0.12 $MPam^{1/2}$ [48]. The $\Delta\sigma_g$ values are 8.2 MPa (5.84% (=8.2/140.5)) and 29 MPa (18.6% (=29/156.1)) for Zr−7085Al and 7TiB_2−7085Al samples, respectively.

With the Zr addition, Al_3Zr dispersoids of high number density and small size are formed in the matrix. Dislocations can either shear or pass by these dispersoids depending on their sizes, which correspond to two kinds of strengthening mechanisms. It has been reported that the transition size from shearing to bypass mechanism in Al−Zr and Al−Sc systems is 4−6 nm [49]. In Fig. 3(f), the average size of Al_3Zr dispersoid is 20 nm, which is larger than the transition size. As a result, the Orowan bypass mechanism is considered for Al_3Zr dispersoids. For TiB_2 particles, it was reported that Orowan bypass mechanism works in the composite [45]. The increase in the YS due to the Orowan strengthening is formulated as follows:

$$\Delta\sigma_{Orowan} = M\frac{0.4Gb}{\pi\sqrt{1-v}}\frac{\ln(2\bar{r}/b)}{\lambda_p} \tag{4}$$

where M is the Taylor factor, which is 3.06 in the present study; v and G are the matrix Poisson ratio and the shear modulus, which are 0.33 and 26.9 GPa, respectively; b is the magnitude of the Al matrix Burgers vector which equals 0.286 nm [48]; $\bar{r}$ is the mean radius of a circular cross-section in a random plane for a spherical precipitate ($\bar{r} = \sqrt{2/3}r$); λ_p is the inter-precipitate spacing. The λ_p measured by Image J software is (150±22) nm. The $\Delta\sigma_{Orowan}$ estimated is 98.8 MPa (70.3% (=98.8/140.5)) for the Zr−7085Al sample [50]. For 7TiB_2−7085Al sample, it is difficult to evaluate the exact Orowan strengthening contribution because TiB_2 particles are not in ideal uniform distribution, and a part of TiB_2 particles are distributed on the GBs with the second phases. This is believed to have the adverse effect on the mechanical strength of composites. The estimated Orowan strengthening contribution is equal to 26−76 MPa (16.7%−48.7% (=26/156.1−76/156.1)), assuming that 20%−70% of TiB_2 particles are well distributed inside the grains.

The overall dislocation will be increased by the introduction of non-deformable particles. It has been observed that dislocation loops are formed around non-deformable particles due to the differences in the elasticity and plasticity of dispersoids and matrix. The dislocations interact with themselves and impede their own motion, which can enhance the yield strength of the material. The increase in yield strength due to improved dislocation density can be depicted using Bailey−Hirsch relationship [51]:

$$\Delta\sigma_d = M\alpha Gb\sqrt{\rho} \tag{5}$$

where α is a constant equal to 0.2, and ρ is the dislocation density. The estimated dislocation strengthening for the Zr−7085Al sample is 33.5 MPa (23.8% (=33.5/140.5)) considering the normalization method. Meanwhile, it has been reported by LIU et al [18] that the increase in the YS due to the dislocation strengthening is about 92 MPa for 5TiB_2−7050Al composite. Here, the estimated dislocation strengthening is 109 MPa (69.8% (=109/156.1)) for the 7TiB_2−7085Al sample assuming that the dislocation increment has an

approximate linear relation with the TiB_2 content.

Conclusively, the addition of TiB_2 particle and Zr can both remarkably enhance the yield strength of the matrix alloy. With 7 wt.% TiB_2 addition, the yield strength of the composite can reach the similar level with the Zr-containing alloy. The main strengthening mechanisms for Zr-containing alloy are the Orowan strengthening (70.3% (=98.8/140.5)) and the dislocation strengthening (23.8% (=33.5/140.5)). Comparably, Orowan strengthening (16.7%−48.7% (=26/156.1−76/156.1)), GB strengthening (18.6% (=29/156.1)) and dislocation strengthening (69.8% (=109/156.1)) should all be taken into consideration for the composite.

4.2.2 Elastic modulus

The Zr addition has little effect on the elastic modulus of the matrix alloy (Table 3). However, it is obvious that the elastic modulus increases steadily as the TiB_2 content increases in the composites. The Tsai−Halpin equation can be used to predict the elastic modulus for the composite (E_c). The equation is as follows [52]:

$$E_c=\frac{E_m(1+2s\eta V_p)}{1-\eta V_p} \tag{6}$$

where E_m (69.2 GPa) is the elastic modulus of the matrix; V_p is the volume content of TiB_2 particle in the composite; s is the particle aspect ratio. Specially, s is assumed to 1 since most TiB_2 particles have cubic or near-spherical shapes. The parameter η can be calculated by the following equation:

$$\eta=\frac{\left(E_p/E_m-1\right)}{\left(E_p/E_m+2s\right)} \tag{7}$$

where E_p (529 GPa) is the elastic modulous of TiB_2 particles.

The calculated elastic moduli of the composites according to the Tsai−Halpin equation are 72.1 GPa for $3TiB_2$−7085Al and 75.6 GPa for $7TiB_2$−7085Al. It is apparent that the estimated results for the composites fit well with the experimental results (Table 3).

5 Conclusions

(1) TiB_2 particles can remarkably refine grain, and the average grain size in the as-cast composite decreases with the increasing TiB_2 content.

(2) TiB_2 particles have the clean interface with the Al matrix. The proper TiB_2 addition may promote recrystallization by the PSN effect. However, these particles can effectively inhibit recrystallization growth and stabilize grain structure. Meanwhile, the Al_3Zr dispersoids can both inhibit recrystallization and stabilize grain structure.

(3) TiB_2 particles can accelerate the aging kinetic of the composite, and the time to reach the peak-aged hardness is shortened by the introduction of TiB_2 particles. Meanwhile, the Zr addition has minor effect on the aging behavior of the material.

(4) TiB_2 particles can give rise to quench sensitivity but can significantly improve the yield strength and ultimate tensile strength of the material. With 3 wt.% TiB_2 addition, the quench sensitivity of the composite can be similar to that of the Zr containing alloy. With 7 wt.% TiB_2 addition, the yield strength and ultimate tensile strength of the composite can be at the same level to those of the Zr-containing alloy.

Acknowledgments

The authors are grateful for the financial supports from the China Postdoctoral Science Foundation (Nos. 2019TQ0193, 2019M661497), the National Key Research and Development Program of China (No. 2018YFB1106302), the National Natural Science Foundation of China (No. 51821001), and the Anhui Provincial Engineering Research Center of Aluminum Matrix Composites, China (No. 2017WAMC002)

References

[1] GUO Z Y, ZHAO G, CHEN X G. Effects of homogenization treatment on recrystallization behavior of 7150 aluminum sheet during post-rolling annealing [J]. Materials Characterization, 2016, 114: 79−87.

[2] LIN Hua-qiang, YE Ling-ying, SUN Lin, XIAO Tao, LIU Sheng-dan, DENG Yun-lai, ZHANG Xin-ming. Effect of three-step homogenization on microstructure and properties of 7N01 aluminum alloys [J]. Transactions of Nonferrous Metals Society of China, 2018, 28: 829−838.

[3] ROBSON J D. A new model for prediction of dispersoid precipitation in aluminium alloys containing zirconium and scandium [J]. Acta Materialia, 2004, 52: 1409−1421.

[4] WLOKA J, VIRTANEN S. Influence of scandium on the

pitting behaviour of Al−Zn−Mg−Cu alloys [J]. Acta Materialia, 2007, 55: 6666−6672.

[5] XIAO Quan-feng, HUANG Ji-wu, JIANG Ying-ge, JIANG Fu-qin, WU Yun-feng, XU Guo-fu. Effects of minor Sc and Zr additions on mechanical properties and microstructure evolution of Al−Zn−Mg−Cu alloys [J]. Transactions of Nonferrous Metals Society of China, 2020, 30: 1429−1438.

[6] LI Bo, PAN Qing-lin, CHEN Cong-ping, YIN Zhi-min. Effect of aging time on precipitation behavior, mechanical and corrosion properties of a novel Al−Zn−Mg−Sc−Zr alloy [J]. Transactions of Nonferrous Metals Society of China, 2016, 26: 2263−2275.

[7] LI Gen, ZHAO Nai-qin, LIU Tao, LI Jia-jun, HE Chun-nian, SHI Chun-sheng, LIU En-zou, SHA Jun-wei. Effect of Sc/Zr ratio on the microstructure and mechanical properties of new type of Al−Zn−Mg−Sc−Zr alloys [J]. Materials Science and Engineering A, 2014, 617: 219−227.

[8] ZHANG Y, BETTLES C, PAUL A R. Effect of recrystallization on Al_3Zr dispersoid behavior in thick plates of aluminium alloy AA7150 [J]. Journal of Materials Science, 2013, 49: 1709−1715.

[9] SCHÖBEL M, PONGRATZ P, DEGISCHER H P. Coherency loss of Al_3(Sc,Zr) precipitates by deformation of an Al−Zn−Mg alloy [J]. Acta Materialia, 2012, 60: 4247−4254.

[10] KANG Lei, ZHAO Gang, WANG Guang-dong, LIU Kun, TIAN Ni. Effect of different quenching processes following solid-solution treatment on properties and precipitation behaviors of 7050 alloy [J]. Transactions of Nonferrous Metals Society of China, 2018, 28: 2162−2172.

[11] LI Cheng-bo, WANG Shao-lin, ZHANG Duan-zheng, LIU Sheng-dan, SHAN Zhao-jun, ZHANG Xin-ming. Effect of Zener−Hollomon parameter on quench sensitivity of 7085 aluminum alloy [J]. Journal of Alloys and Compounds, 2016, 688: 456−462.

[12] WANG Ming-liang, CHEN Dong, CHEN Zhe, WU Yi, WANG Fei-fei, MA Nai-heng, WANG Hao-wei. Mechanical properties of in-situ TiB_2/A356 composites [J]. Materials Science and Engineering A, 2014, 590: 246−254.

[13] MA Y, CHEN Z, WANG M L, CHEN D, MA N H, WANG H W. High cycle fatigue behavior of the in-situ TiB_2/7050 composite [J]. Materials Science and Engineering A, 2015, 640: 350−356.

[14] LIU Zhi-wei, DONG Zhi-wu, CHENG Xiao-le, ZHENG Qiao-ling, ZHAO Jing-rui, HAN Qing-you. On the supplementation of magnesium and usage of ultrasound stirring for fabricating in situ TiB_2/A356 composites with improved mechanical properties [J]. Metallurgical and Materials Transactions A, 2018, 49: 5585−5598.

[15] MA Y, ADDAD A, JI G, ZHANG M X, LEFEBVRE W, CHEN Z, JI V. Atomic-scale investigation of the interface precipitation in a TiB_2 nanoparticles reinforced Al−Zn−Mg−Cu matrix composite [J]. Acta Materialia, 2020, 185: 287−299.

[16] TANG Y, CHEN Z, BORBELY A, JI G, ZHONG S Y, SCHRYVERS D, WANG H W. Quantitative study of particle size distribution in an in-situ grown Al–TiB_2 composite by synchrotron X-ray diffraction and electron microscopy [J]. Materials Characterization, 2015, 102: 131−136.

[17] XIONG Yi-feng, WANG Wen-hu, SHI Yao-yao, JIANG Rui-song, LIN Kun-yang, LIU Xiao-fen. Fatigue behavior of in-situ TiB_2/7050Al metal matrix composites: Fracture mechanisms and fatigue life modeling after milling [J]. International Journal of Fatigue, 2020, 138: 105698.

[18] LIU Gen, GENG Ji-wei, LI Yu-gang, CAI Li, WANG Ming-liang, CHEN Dong, MA Nai-heng, WANG Hao-wei. Effects of pre-strain on the microstructural evolution and mechanical strength of in situ TiB_2/7050 Al composite [J]. Advanced Engineering Material, 2019, 21: 1900042.

[19] SHEN Yan-wei, LI Xian-feng, HONG Tian-ran, GENG Ji-wei, WANG Hao-wei. Effects of TiB_2 particles on microstructure and mechanical properties of an in-situ TiB_2−Al−Cu−Li matrix composite [J]. Materials Science and Engineering A, 2016, 655: 265−268.

[20] CHEN Fei, CHEN Zong-ning, MAO Feng, WANG Tong-min, CAO Zhi-qiang. TiB_2 reinforced aluminum based in situ composites fabricated by stir casting [J]. Materials Science and Engineering A, 2015, 625: 357−368.

[21] ZHANG Li-li, JINAG Hong-xiang, HE Jie, ZHAO Jiu-zhou. Kinetic behaviour of TiB_2 particles in Al melt and their effect on grain refinement of aluminium alloys [J]. Transactions of Nonferrous Metals Society of China, 2020, 30: 2035−2044.

[22] LIU Yan, JIANG Da-ming, XIE Wen-long, HU Jie, MA Bo-ran. Solidification phases and their evolution during homogenization of a DC cast Al−8.35Zn−2.5Mg−2.25Cu alloy [J]. Materials Characterization, 2014, 93: 173−183.

[23] SHE Huan, SHU Da, DONG An-ping, WANG Jun, SUN Bao-de, LAI Hong-chang. Relationship of particle stimulated nucleation, recrystallization and mechanical properties responding to Fe and Si contents in hot-extruded 7055 aluminum alloys [J]. Journal of Materials Science & Technology, 2019, 35: 2570−2581.

[24] SCHAFFER P L, MILLER D N, DAHLE A K. Crystallography of engulfed and pushed TiB_2 particles in aluminum [J]. Scripta Materialia, 2007, 57: 1129−1132.

[25] GENG Ji-wei, HONG Tian-ran, MA Yu, WANG Ming-liang, CHEN Dong, MA Nai-heng, WANG Hao-wei. The solution treatment of in-situ sub-micron TiB_2/2024 Al composite [J]. Materials and Design, 2016, 98: 186−193.

[26] SHA G, CEREZO A. Early-stage precipitation in Al−Zn−Mg−Cu alloy (7050) [J]. Acta Materialia, 2004, 52: 4503−4516.

[27] DU Rui, GAO Qi, WU Shu-sen, LU Shu-lin, ZHOU Xiong. Influence of TiB_2 particles on aging behavior of in-situ TiB_2/Al−4.5Cu composites [J]. Materials Science and Engineering A, 2018, 721: 244−250.

[28] LI Pei-yue, XIONG Bai-qing, ZHANG Yong-an, LI Zhi-hui, ZHU Bao-hong, WANG Feng, LIU Hao-wei. Quench

sensitivity and microstructure character of high strength AA7050 [J]. Transactions of Nonferrous Metals Society of China, 2012, 22: 268−274.

[29] NEWKIRK J W, MACKENZIE D S. The Jominy end quench for light-weight alloy development [J]. Journal Materials Engineering and Performance, 2000, 9: 408−415.

[30] DENG Yun-lai, WAN Li, ZHANG Yun-ya, ZHANG Xing-ming. Influence of Mg content on quench sensitivity of Al−Zn−Mg−Cu aluminum alloys [J]. Journal of Alloys and Compounds, 2011, 509: 4636−4642.

[31] NIE Bao-hua, LIU Pei-ying, ZHOU Tie-tao. Effect of compositions on the quenching sensitivity of 7050 and 7085 alloys [J]. Materials Science and Engineering A, 2016, 667: 106−114.

[32] LIU Sheng-dan, LI Cheng-bo, DENG Yun-lai, ZHANG Xin-ming. Influence of grain structure on quench sensitivity relative to localized corrosion of high strength aluminum alloy [J]. Materials Chemistry and Physics, 2015, 167: 320−329.

[33] THOMAS M P, KING J E. Quench sensitivity of 2124 Al alloy and Al/SiC_p metal matrix composite [J]. Scripta Metallurgica et Materialia, 1994, 31: 209−214.

[34] OGUOCHA I N A, RADJABI M, YANNACOPOULOS S. The effect of cooling rate on the quench sensitivity of 2618 Al/Al_2O_3 MMC [J]. Journal of Materials Science, 2000, 35: 5629−5634.

[35] NAFAR D J, ANBARLOOIE B, MIETTNEN A, HOSSEINI T H, REMES H. Effects of particle clustering on the plastic deformation and damage initiation of particulate reinforced composite utilizing X-ray CT data and finite element modeling [J]. Composites: Part B, 2018, 153: 57−69.

[36] SUN Zhi-chao, ZHENG Li-shuang, YANG He. Softening mechanism and microstructure evolution of as-extruded 7075 aluminum alloy during hot deformation. [J]. Materials Characterization, 2014, 90: 71−80.

[37] REZAEI ASHTIANI H R, SHAHSAVAR P. Constitutive modeling of flow behavior of precipitation-hardened AA7022-T6 aluminum alloy at elevated temperature [J]. Transactions of Nonferrous Metals Society of China, 2020, 30: 2927−2940.

[38] SUN Z C, WU H L, CAO J, YIN Z K. Modeling of continuous dynamic recrystallization of Al−Zn−Cu−Mg alloy during hot deformation based on the internal-state-variable (ISV) method [J]. International Journal of Plasticity, 2018, 106: 73−78.

[39] SAKAI T, BELYAKOV A, KAIBYSHEV R, MIURA H, JONAS J. Dynamic and post-dynamic recrystallization under hot, cold and severe plastic deformation conditions [J]. Progress in Materials Science, 2014, 60: 130−207.

[40] LIU Jing, YAO Pei, ZHAO Nai-qin, SHI Chun-sheng, LI Hui-jun, LI Xuan, XI De-sheng, YANG Shuo. Effect of minor Sc and Zr on recrystallization behavior and mechanical properties of novel Al−Zn−Mg−Cu alloys [J]. Journal of Alloys and Compounds, 2016, 657: 717−725.

[41] DENG K K, WANG X J, ZHENG M Y, WU K. Dynamic recrystallization behavior during hot deformation and mechanical properties of 0.2 μm SiC_p reinforced Mg matrix composite [J]. Materials Science and Engineering A, 2013, 560: 824−830.

[42] ROBSON J D, HENRY D T, DAVIS B. Particle effects on recrystallization in magnesium−manganese alloys: Particle-stimulated nucleation [J]. Acta Materialia, 2009, 57: 2739−2747.

[43] ZHANG Yong-hao, JENSEN J D, ZHANG Yu-bin, LIN Feng-xiang, ZHANG Zhi-qing, LIU Qing. Three-dimensional investigation of recrystallization nucleation in a particle-containing Al alloy [J]. Scripta Materialia, 2012, 67: 320−323.

[44] HUANG K, MARTHINSEN K, ZHAO Q L, LOGE R E. The double-edge effect of second phase particles on the recrystallization behaviour and associated mechanical properties of metallic materials [J]. Progress in Materials Science, 2018, 92: 284−359.

[45] LI He, WANG Xiao-ming, CHAI Li-hua, WANG Hai-jing, CHEN Zi-yong, XIANG Zhi-lei, JIN Tou-nan. Microstructure and mechanical properties of an in-situ TiB_2/Al−Zn−Mg−Cu−Zr composite fabricated by melt-SHS process [J]. Materials Science and Engineering A, 2018, 720: 60−68.

[46] XIAO Peng, GAO Yi-min, YANG Cui-cui, LIU Zhi-wei, LI Ye-fei, XU Fei-xing. Microstructure, mechanical properties and strengthening mechanisms of Mg matrix composites reinforced with in situ nanosized TiB_2 particles [J]. Materials Science and Engineering A, 2018, 710: 251−259.

[47] FAN Cai-he, OU Ling, HU Ze-yi, YANG Jian-jun, CHEN Gang, YAN Hong-ge. Microstructures and mechanical properties of BP/7A04Al matrix composites [J]. Transactions of Nonferrous Metals Society of China, 2019, 29: 2027−2034.

[48] MA K K, HU T, YANG H, TOPPING T, YOUSEFIANI A, LAVERNIA E J, SCHOENUNG J M. Coupling of dislocations and precipitates: Impact on the mechanical behavior of ultrafine grained Al−Zn−Mg alloys [J]. Acta Materialia, 2009, 103: 153−164.

[49] SEIDMAN D N, MARQUIS E A, DUNAND D C. Precipitation strengthening at ambient and elevated temperatures of heat-treatable Al(Sc) alloys [J]. Acta Materialia, 2002, 50: 4021−4035.

[50] SENKOV O N, SHAGIEV M R, SENKOVA S V, MIRACLE D B. Precipitation of Al_3(Sc,Zr) particles in an Al−Zn−Mg−Cu−Sc−Zr alloy during conventional solution heat treatment and its effect on tensile properties [J]. Acta Materialia, 2008, 56: 3723−3738.

[51] MIRZA F A, CHEN D L. A unified model for the prediction of yield strength in particulate-reinforced metal matrix nanocomposites [J]. Materials, 2015, 8: 5138−5153.

[52] AFFDL J C H, KARDOS J L. The Halpin−Tsai equations: A review [J]. Polymer Engineering and Science, 1976, 16: 344−352.

纳米 TiB_2 颗粒和 Al_3Zr 粒子对 Al−Zn−Mg−Cu 基材料显微组织和力学性能的影响

肖宏宇[1,2]，李宇罡[1,2]，耿继伟[1,2,3]，李红萍[4]，汪明亮[1]，陈 东[1,2,3]，李铸国[5]，王浩伟[1]

1. 上海交通大学 金属基复合材料国家重点实验室，上海 200240；
2. 上海交通大学 材料科学与工程学院，上海 200240；
3. 安徽省铝基复合材料工程研究中心，淮北 235000；
4. 上海飞机设计研究院，上海 201203；
5. 上海交通大学 上海市激光制造与材料改性重点实验室，上海 200240

摘 要：采用多尺度显微组织表征技术研究 TiB_2 和 Al_3Zr 对热挤压 Al−Zn−Mg−Cu 基材料的显微组织、时效响应和力学性能的影响。结果表明，添加适量 TiB_2 颗粒在凝固过程中能有效细化晶粒，挤压过程中能促进动态再结晶，固溶过程中能有效抑制晶粒长大。同时，与无 Zr 合金相比，Zr 元素的添加在凝固过程在对晶粒细化无明显影响，但可以有效抑制再结晶和晶粒长大。TiB_2 颗粒能加快材料的时效动力学并且提高峰时效硬度；Zr 元素也能提高材料的峰时效硬度，但对时效动力学无明显影响。最后，分析不同材料的淬火敏感性、弹性模量和拉伸性能，并研究此类材料显微组织与力学性能之间的关系及其强化机理。

关键词：TiB_2；Al_3Zr；显微组织；时效动力学；力学性能

(Edited by Wei-ping CHEN)